Advances in Geo-Energy Research

Vol. 17, No. 3, p. 241-255, 2025

Original article

Nanomechanics and pore structure evolution in organic-rich shale reservoirs during high-temperature treatment: A multi-scale analysis of microscopic stability

Qiuqi Chen[1], Xin Tang[1]*, Ying Shi[2], Ruigang Zhang[3], Fuhua Shang[4]

[1]*School of Civil Engineering, Chongqing Three Gorges University, Chongqing 404199, P. R. China*

[2]*Department of Earth Resources Engineering, Faculty of Engineering, Kyushu University, Fukuoka 819-0395, Japan*

[3]*Chongqing Key Laboratory of Resource and Environmental Effects of Major Geological Events (Chongqing Institute of Geology and Mineral Resources), Chongqing 401120, P. R. China*

[4]*School of Resource and Environmental Engineering, Inner Mongolia University of Technology, Neimenggu 010051, P. R. China*

Keywords:
Shale reservoir
thermal treatment
atomic force microscopy
geometric stability
spatial statistics

Cited as:
Chen, Q., Tang, X., Shi, Y., Zhang, R., Shang, F. Nanomechanics and pore structure evolution in organic-rich shale reservoirs during high-temperature treatment: A multi-scale analysis of microscopic stability. Advances in Geo-Energy Research, 2025, 17(3): 241-255.
https://doi.org/10.46690/ager.2025.09.06

Abstract:
To address the challenges of conflicting macroscopic mechanical tests and the inability to reveal complex nanoscale mechanisms during deep shale thermal modification, this study comprehensively investigates the microstructural and nanomechanical evolution of Longmaxi shale under heat treatment. This involves the innovative combination of gas adsorption, atomic force microscope high-resolution mapping, and multi-level spatial statistical analysis to systematically elucidate the spatial evolution of the pore structure of shale, surface morphology, and nanomechanical properties. The findings reveal a unique hardening-softening-rehardening three-stage pattern: From 25-400 °C, the average reduced modulus increases due to dehydration; from 400-600 °C, organic matter pyrolysis significantly decreases the modulus, with intense atomic force microscope topographic uplift; from 600-900 °C, the modulus slightly increases again due to structural collapse and pore network regeneration. Local indicators of spatial association analysis shows that this macro evolution stems from synergistic microscopic phase space reshaping. Crucially, the mesopore volume increases most significantly in the 400-500 °C range, and it exhibits its most notable increase. Considering energy efficiency and feasibility, this study demonstrates for the first time that 400-500 °C is an ideal temperature window for effective organic matter pyrolysis and nanopore optimization from a nanoscale spatial distribution and geometric stability perspective. This work provides crucial micro-mechanical mechanism support and precise temperature guidance for deep shale thermal modification, significantly outperforming the temperature ranges from traditional macroscopic experiments and filling the gap in macro-nanoscale mechanical discrepancies and spatial feature analysis.

1. Introduction

Organic-rich carbonaceous shale plays an indispensable bridging role in promoting the clean and efficient utilization of fossil fuels due to its immense resource potential (Song et al., 2017; Cheng et al., 2025). However, the effective development of such reservoirs faces significant challenges. Their characteristic of source-reservoir integration results in an extremely dense matrix (Cai et al., 2022b; Wang et al., 2023b; Feng et al., 2025), where the storage and seepage space

Yandy Scientific Press

*Corresponding author.
E-mail address: Qiuqi_C@126.com (Q. Chen); tangxin@cumt.edu.cn (X. Tang); shi.ying.902@s.kyushu-u.ac.jp (Y. Shi); sportagang@163.com (R. Zhang); fhshangcumt@163.com (F. Shang).

Received July 19, 2025; revised August 15, 2025; accepted September 2, 2025; available online September 5, 2025.

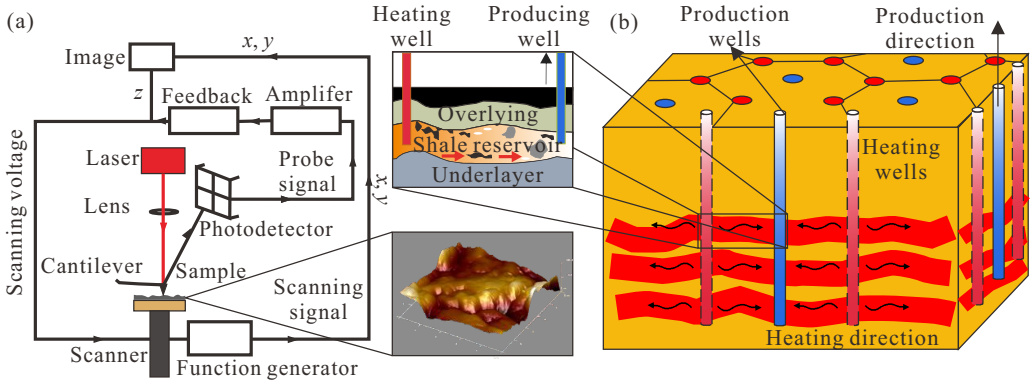

Fig. 1. Research methodology and engineering applications (Chen et al., 2025): (a) AFM and (b) *in-situ* conversion.

is primarily composed of micron- to nanometer-scale pore networks, making fluid transport extremely difficult (Loucks et al., 2012; Iqbal et al., 2021; Cai et al., 2022a).

To overcome the above bottleneck, *in-situ* thermal alteration technology for carbonaceous shale reservoirs has been developed (Jiang et al., 2007) (Fig. 1). This technology, which involves heating the subsurface reservoir, aims to enhance organic matter conversion rates, improve fluid properties, and create new flow pathways (Saif et al., 2017; Wang et al., 2021). This process induces a series of complex physicochemical transformations, including organic matter pyrolysis and mineral phase transitions, causing the mechanical properties of shale to exhibit complex, non-linear, and anisotropic behavior (Li et al., 2022; Zhang et al., 2025). The mechanical stability of carbonaceous shale is therefore a crucial factor that directly determines whether an effective fracture network can be formed and maintained during the thermal recovery process.

Currently, such mechanical properties are evaluated by macroscopic rock mechanical tests such as uniaxial and triaxial compression (Sun et al., 2023; Liu et al., 2025). Previous studies have extensively investigated the effects of heat treatment on the mechanical properties of carbonaceous shale. High-temperature triaxial compression tests demonstrated that differences in the thermal expansion coefficients of mineral particles can cause inconsistent expansion across grain boundaries, which generates additional thermal stress and reduces the bearing capacity of specimens. Some studies reported a softening effect: Asphaltenes become more compliant upon heating, and higher temperatures are associated with a reduction in elastic modulus. (Zargari et al., 2016; Emmanuel et al., 2017), while mineral phase transformations promote microcrack formation (Li et al., 2020). Conversely, other studies observed an opposite trend, namely an increase in strength (Khatibi et al., 2018; Vranjes-Wessely et al., 2021). These discrepancies highlight the limitations of macroscopic average measurements and indicate that the heat treatment of shale is a complex, multi-stage process that cannot be captured by simple linear models. To address these limitations, nanoindentation and atomic force microscope (AFM) have been commonly employed to characterize micro- and nanoscale alterations (Wang et al., 2023a; Wang et al., 2025; Yan et al., 2025). AFM collects force-displacement curves at each pixel, allowing researchers to infer local elasticity, stiffness, dissipation, and adhesion (Graham et al., 2021). This method requires only small sample volumes, significantly reducing resource consumption (Zhang et al., 2018). Furthermore, it enables the three-dimensional mapping of surface height, roughness, and modulus based on tip-sample interactions. For example, Emmanuel et al. (2016) examined the changes in the elastic properties of shale organic matter with thermal maturity, while Goodarzi et al. (2017) used peakforce-quantitative nanomechanical mapping (QNM) to validate homogenization models of organic-rich shale. Similarly, Li et al. (2018) investigated the nanomechanical properties of high-maturity solid bitumen, and Dickinson et al. (2016) employed AFM probe technology to map adhesion curves between crude oil and carbonate minerals, providing insights into reservoir-fluid interactions. In Dai et al. (2024)'s study, AFM characterization was employed to assess shale micro-morphology and elemental distribution, which revealed the effect of CO_2 on surface wettability under reservoir conditions.

Despite these advances, macroscopic mechanical tests can only provide an overall average response and fail to reveal the complex spatial interactions at the nanoscale. They cannot answer the critical question of how the mechanical properties of different components are spatially organized, and whether there are spatial autocorrelations and clustering patterns among them, features that are central to understanding how heat treatment induces microcracks and weakens the skeletal structure. Existing micromechanical studies have observed the effect of temperature on shale properties (Emmanuel et al., 2016); however, they are generally limited to the statistical evaluation of average properties or traditional image segmentation. As a result, they lack in-depth analysis of how surface roughness, pore structure and mechanical properties interact, and rarely address the spatial patterns or correlations of multiphase components (Giergiel et al., 2022; Wang and Cheng, 2023; Paruchuri et al., 2024). To address these shortcomings, in this work, shale samples from the Longmaxi Formation were subjected to stepwise thermal treatment (25-900 °C) under vacuum conditions, simulating deep shale reservoirs. To comprehensively analyze high-resolution AFM data, we systematically integrate spatial statistical methods, performing multi-level spatial autocorrelation analysis through both global Moran's index and local indicators of spatial association (Cliff and Ord, 1973; Anselin, 1995). The primary goal of this

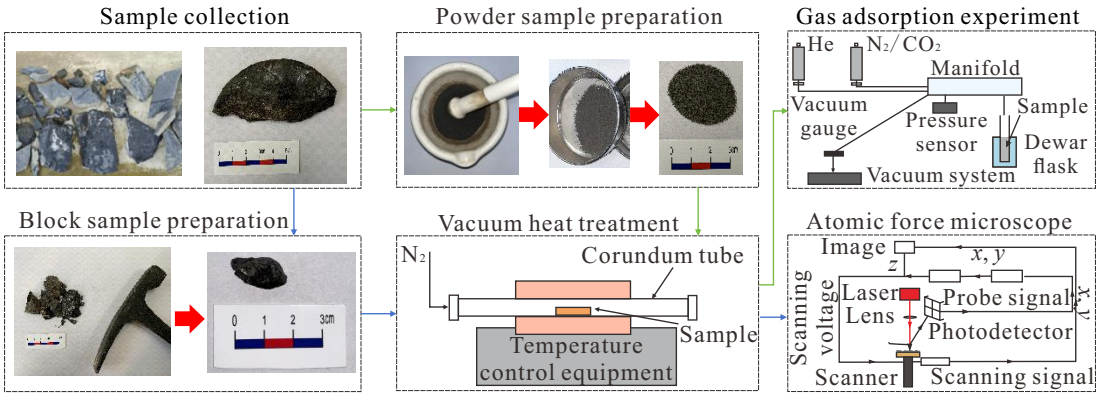

Fig. 2. Shale sample preparation and experiments.

unified methodology is to enable a quantitative interpretation of thermal alteration's spatial arrangement, derived from high-resolution topographical and mechanical property mapping. The ultimate goal is to characterize the complex damage and reconstruction mechanisms of post-alteration shale by constructing an analytical model that links mechanics, topography and geometric stability, and can thereby precisely identify the optimal alteration temperature threshold in the thermal treatment process.

2. Experimental method

2.1 Sample preparation

The shale samples were collected from an outcrop of the Longmaxi Formation in Longtan Town, Youyang County, Chongqing, China (108°52′48.482″E, 28°38′51.727″N). The organic-rich carbonaceous shale selected in this study has unclear horizontal and vertical bedding structures, which is different from typical anisotropic shales. To minimize the influence of the inherent heterogeneity of shale, which arises from its complex structure and mineralogy, both powder and block samples were prepared from the same parent rock. A fresh outcrop section, selected for its structural integrity and the absence of visible fractures and impurities, was used for all sample preparations. A portion of the parent rock was manually crushed to create ten block samples, each with all dimensions less than 1 cm. The remaining fragments were further processed and screened using standard test sieves to obtain powdered samples with a particle size range of 150-200 μm. These powdered samples were then divided into ten groups, with each group weighing approximately 2 g (Fig. 2).

To simulate deep shale geological settings, all samples (both powdered and block) underwent a stepwise thermal treatment protocol under vacuum conditions. The target temperatures were set at 100 °C intervals from 25 °C (room-temperature control) up to 900 °C. During the procedure, the samples were heated at a constant rate of 10 °C/min to each target temperature and then held isothermally for 360 min. Upon treatment completion, the samples cooled naturally to room temperature while remaining in the furnace. To eliminate any potential influence from procedural variations on the experimental results, the same thermal treatment protocol was applied to the block AFM samples and the powdered samples.

2.2 Gas adsorption experiments

The low-temperature carbon dioxide (CO_2) and nitrogen (N_2) adsorption isotherms were measured to characterize the pore structure of the samples. The CO_2 adsorption experiment was performed at 273.15 K over a relative pressure (P/P_0) range of 0.0005-0.03, and the low-temperature N_2 adsorption experiment was performed at 77.35 K over a P/P_0 range of 0.01-0.99. Pores were classified according to the IUPAC standard into micropores (< 2 nm), mesopores (≥ 2 nm, ≤ 50 nm), and macropores (> 50 nm). To obtain the micropore volume, the Dubinin-Radushkevich model was employed with CO_2 adsorption data. Conversely, N_2 adsorption data were analyzed using the Barrett-Joyner-Halenda (BJH) model to establish the mesopore volume.

2.3 AFM Experiments

The shale samples were first fixed using a cold-mounting technique. Small shale fragments (< 1 cm) were placed in molds, into which epoxy resin was poured for cold mounting. After the resin cured, operable sample blocks were obtained. Subsequently, the mounted samples were subjected to mechanical grinding and polishing.

Nanomechanical properties and surface topography were characterized using an AFM operating in QNM mode. All measurements were conducted under controlled ambient conditions (25 ± 1 °C temperature) to ensure data consistency. For each sample, a total of twenty-five independent 5×5 μm^2 areas were scanned at a resolution of 256×256 pixels. The representativeness of the selected regions at the macroscopic scale and the randomness at the microscopic scale were ensured. The statistical robustness of the results and the effective capture of the heterogeneity characteristics of the material were ascertained by performing statistical analysis on the nanoscale data from these 25 regions.

The nanomechanical properties of samples were measured using the QNM mode. To interpret the force-indentation behavior, the Derjaguin-Muller-Toporov model (Derjaguin et al., 1975) was employed. Within this model, the correlation between the applied force and the indentation depth is expressed as follows:

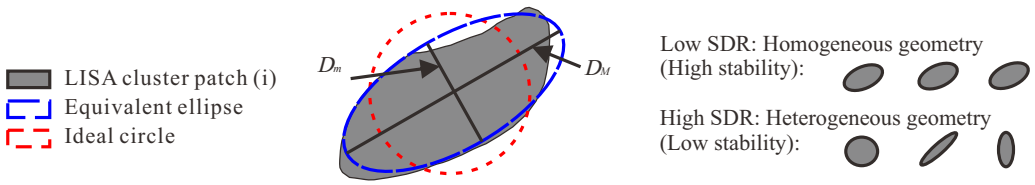

Fig. 3. Schematic of LISA cluster geometric stability (SDR).

$$F = \frac{4}{3}E^*\sqrt{R\delta^3} + F_a \tag{1}$$

where F represents the applied force, R represents the probe tip radius of curvature, δ represents the indentation depth, F_a represents the adhesion force, and E^* represents the reduced modulus. This value serves as a reliable indicator of the elastic properties of the material.

E^* is defined by considering the combined elastic contributions of both the sample and the probe:

$$\frac{1}{E^*} = \frac{1-\nu_p^2}{E_p} + \frac{1-\nu_s^2}{E_s} \tag{2}$$

where ν_s and E_s denote Poisson's ratio and the Young's modulus of the sample, while E_P and ν_p correspond to those of the probe tip, respectively. In this work, E^* values obtained from the model were used as the basis for all subsequent analyses, including spatial statistical evaluations. AFM measurements were carried out on twenty-five distinct regions of 5×5 μm^2, each captured at a resolution of 256×256 pixels.

2.4 Nanomechanical spatial distribution analysis

This study carried out spatial autocorrelation analysis, utilizing global Moran's index (I) and local indicators of spatial association (LISA), to investigate the overall spatial distribution patterns and local clustering characteristics on the sample surface (Moran, 1950). To gauge the total spatial autocorrelation of an attribute over an entire study area, I is employed. This index reveals whether like values (e.g., high or low) display patterns of spatial aggregation, scattering, or randomness. The calculation of I follows the formula:

$$I = \frac{N}{\sum_{i=1}^{N}\sum_{j=1}^{N} w_{ij}} \frac{\sum_{i=1}^{N}\sum_{j=1}^{N} w_{ij}(x_i-\bar{x})(x_j-\bar{x})}{\sum_{j=1}^{N}(x_i-\bar{x})^2} \tag{3}$$

where I represents the global Moran's index; N represents the total number of pixels; x_i and x_j denote the attribute values at pixels i and j, respectively; w_{ij} represents the spatial weight that quantifies the proximity between pixels i and pixel j; and $\bar{x}$ is the mean value of the attribute across all pixels.

For a spatial unit i, its local Moran's index (I_i) is defined as follows (Anselin, 1995):

$$I_i = \frac{(m_i-\bar{m})}{S^2}\sum_{\substack{j=1 \\ j\neq i}}^{N} K_{ij}(m_j-\bar{m}) \tag{4}$$

where $\bar{m}$ denotes the overall mean of the location attribute; m_i denotes the attribute value at location i; m_j is the attribute value at location j; K_{ij} represents the spatial weight representing the spatial relationship between location i and location j; and S^2 is the sample variance of the attribute.

Given the grid-like, regular arrangement characteristics of AFM nanomechanical mapping data, we employed a proximity-based weighting matrix, specifically utilizing a Queen Contiguity weighting matrix. The constructed weighting matrix is inherently sparse, meaning that each cell (pixel) is considered spatially associated with all eight of its direct neighbors (including horizontal, vertical, and diagonal directions), which significantly improves the computational efficiency.

The core operation of local indicators of spatial association is to evaluate the statistical significance of each local index (I_i). This significance test, when combined with the signs of both a location's deviation from the overall mean and its corresponding spatial lag, is used to classify the spatial pattern as either clustering or an outlier.

2.5 Sectional geometric stability analysis

To quantitatively evaluate the geometric morphology of the LISA spatial clusters, this study introduces the standard deviation of the relative area deviation (SDR) as a key metric (Lovric, 2025). SDR is a dimensionless parameter that quantifies the shape uniformity of the LISA spatial clusters, thereby reflecting the geometric stability of their spatial pattern (Fig. 3):

$$\sigma_R = \sqrt{\frac{1}{H-1}\sum_{i=1}^{H}(R_i-\mu_R)^2} \tag{5}$$

where σ_R represents SDR, R_i represents the relative deviation of the area of the i-th cluster (Eq. (6)), μ_R represents the mean of the relative area deviations (Eq. (7)), H is the total number of independent clusters identified for a specific type of LISA cluster.

R_i defined as:

$$R_i = \frac{|A_i - A_c|}{A_c} \tag{6}$$

where A_i denotes the area of the i-th cluster, and A_c denotes the ideal circular area (Eq. (9)).

μ_R is defined as:

$$\mu_R = \frac{1}{H}\sum_{i=1}^{N} R_i \tag{7}$$

The area of this equivalent ellipse, A_e, is calculated from its major and minor axes as follows:

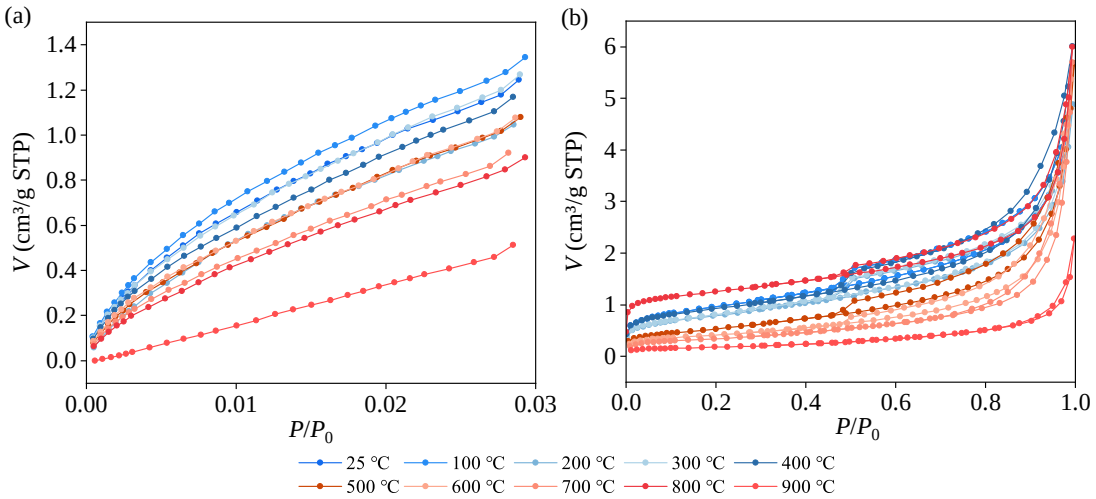

Fig. 4. Gas adsorption-desorption isotherms of shale after thermal treatment: (a) CO_2 at 273 K and (b) N_2 at 77 K.

$$A_e = \frac{\pi D_M D_m}{4} \tag{8}$$

where D_M and D_m are the major and minor axes of a patch's equivalent ellipse, respectively (Fig. 3).

The ideal circular standard area, A_c, is defined as follows:

$$A_c = \pi \left(\frac{D_M + D_m}{4} \right)^2 \tag{9}$$

In this study, both the SDR (sectional geometric stability analysis) and Moran's index (nanomechanical spatial distribution analysis) were applied directly to nanomechanical mapping data obtained through high-resolution AFM. Moran's index is utilized to examine spatial clustering patterns and topological arrangements across a surface. Within the complete scanned area, it effectively elucidates the overall spatial autocorrelation and specific local clustering behaviors of nanomechanical parameters. SDR, on the other hand, focuses on the local geometric stability and heterogeneity characteristics along a line, quantitatively evaluating the geometric morphology and shape uniformity of LISA spatial clusters (i.e., local clusters identified by Moran's index analysis). The combination of these two methods allows for a more comprehensive description of the heterogeneity of shale nanomechanical properties and their spatial distribution patterns at the nanoscale. Through this integrated analysis, we could not only identify regions where nanomechanical properties are clustered but also quantify the geometric stability and heterogeneity characteristics of these regions, thereby providing a deeper and more comprehensive understanding of the complex structure and mechanical response of shale at the nanoscale.

3. Results

3.1 Gas adsorption experiments

Gas adsorption experiments were conducted on the thermally treated samples. By analyzing the CO_2 (273 K) adsorption and low-temperature N_2 (77 K) data (Fig. 4), the mesopore and micropore structures of the samples treated at different temperatures (from 25 to 900 °C in 100 °C intervals) were separately characterized, and the evolution patterns of the pore structure parameters derived from these experiments were comprehensively evaluated.

The results show that, at the baseline temperature of 25 °C, the pristine shale sample exhibits a composite pore structure characterized by the coexistence of micropores and mesopores, and its total Brunauer-Emmett-Teller (BET) (Brunauer et al., 1938) specific surface area is 3.390 m^2/g. The total pore volume is dominated by mesopores, which have a volume of 0.00559 cm^3/g (accounting for 63.09%), while the micropore volume is 0.00327 cm^3/g (accounting for 36.91%). This initial state serves as the baseline for all subsequent thermal treatments.

Up to 400 °C, the shale's pore structure shows no significant changes. At 400 °C, the pore structure develops to an optimal state. This is evidenced by a sharp expansion of the mesopore volume to its maximum value of 0.00625 cm^3/g, an 11.8% increase relative to the 25 °C baseline. Concurrently, the proportion of mesopores within the total pore volume also reaches its peak at 68.76%, significantly strengthening their dominant role (Fig. 5(a)). This observation is consistent with the BJH mesopore specific surface area, which also peaks at 400 °C (3.45866 m^2/g). In contrast, the micropore volume continuously decreases during this stage, reaching 0.00284 cm^3/g. From 400 to 700 °C, the BET specific surface area experiences a sharp decay from 3.228 to 1.219 m^2/g, a substantial decrease of 62.2% (Fig. 5(b)). Both micropore and mesopore volumes also undergo an irreversible reduction, declining to 0.00221 cm^3/g and 0.00413 cm^3/g, respectively.

A key anomaly occurs at 800 °C: Despite the continued reduction in both micropore and mesopore volumes, the BET specific surface area anomalously surges to its overall maximum of 4.057 m^2/g. This constitutes a significant increase in BET surface area within this temperature range. Supplementary nitrogen adsorption experiment at 850 °C shows that the BET specific surface area decreases sharply between 800-900 °C (Fig. 5(b)), which is consistent with observations by Chen et al. (2024) in their adsorption study of thermally

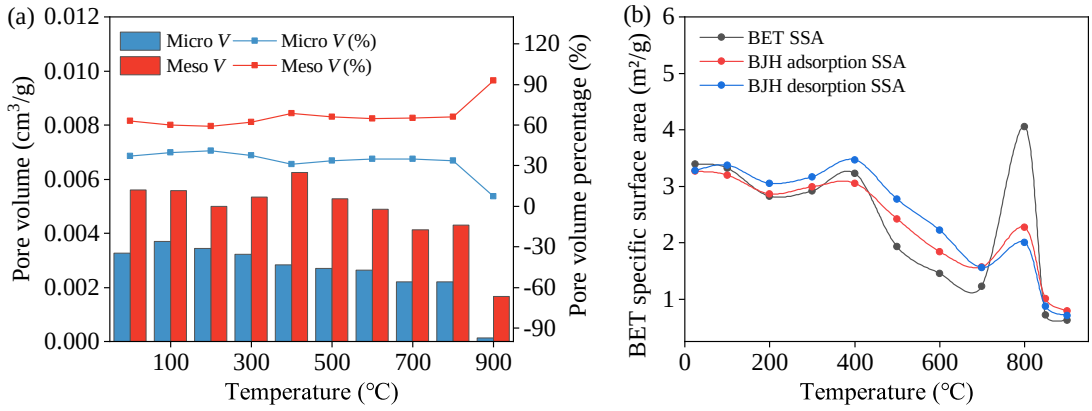

Fig. 5. Evolution of shale pore structure with temperature: (a) Micropore, mesopore volumes and proportions and (b) BET surface area.

treated shale. However, the BJH specific surface area, which primarily reflects mesopores, does not increase concurrently. This suggests that the peak in BET surface area does not originate from an increase in accessible, effective porosity but rather from the generation of numerous disconnected, ultrafine pores or a highly complex surface morphology resulting from structural collapse and reconstruction.

3.2 AFM results

To directly visualize the progressive changes in surface micromorphology and to numerically assess the modifications to topological features, thermally treated shale samples underwent characterization using AFM. Guided by the results of the gas adsorption experiments, representative AFM topography maps of the shale samples at key temperature points are presented in Fig. 6.

The analysis of surface roughness and its corresponding statistical parameters reveals distinct stages of topographical evolution (Fig. 7). Initially, in the temperature range of 25 to 500 °C, both the arithmetic mean roughness (R_a) and the root mean square roughness (R_q) continuously decrease, reaching their minimum at 500 °C ($R_a = 73.33$ nm). As the temperature rises from 500 °C to 600 °C, the surface roughness undergoes an abrupt change, with R_a and R_q values surging to their overall peak values ($R_a = 311.04$ nm), indicating a significant increase in surface irregularity.

Changes in the morphological parameters, skewness (R_s) and kurtosis (R_k), provide further details about the surface structure. Following the peak roughness observed at 600 °C, the surface undergoes further significant topological changes. At 700 °C, the skewness (R_s) reaches an extremely negative value of -0.9678, indicating that the surface has transformed into a structure dominated by deep valleys or pores following intense reconstruction. Subsequently, at higher temperatures (800-900 °C), the R_s value approaches zero. Concurrently, the kurtosis (R_k) becomes significantly negative at 900 °C (-0.8176). Taken together, these parameters suggest that the surface ultimately evolves into a wavy topography characterized by large undulations but with rounded peaks and valleys and a relatively uniform distribution.

4. Discussion

4.1 Evolution of spatial orderliness in shale

Four nanomechanical parameters of the thermally altered shale underwent global spatial autocorrelation analysis. Throughout the entire range of temperatures evaluated, these parameters exhibited a statistically significant positive global spatial autocorrelation (all Moran's index > 0.7) (Fig. 8). This indicates that the nanomechanical properties of shale have a consistent spatial clustering pattern: Hard regions tend to be adjacent to other hard regions and soft regions to other soft regions. This phenomenon of like attracts like persists throughout the process, suggesting that the inherent spatial clustering structure of shale, composed of organic matter and mineral components, is inherited even after undergoing drastic physicochemical changes. The average E^* (GPa) reveals a unique three-stage evolution pattern: rapid hardening-pyrolytic softening-rehardening.

Stage 1 (25-400 °C): Dehydration consolidation and initial hardening. The E^* of the shale increases sharply from a very low value of 0.76 GPa at room temperature to a peak of 3.77 GPa at 400 °C (Fig. 8(d)). Concurrently, energy dissipation plummets from an initial 8,029 to 401.8 eV at 300 °C (Fig. 8(b)), and adhesion force drops from 5.90 to 0.26 nN at 300 °C (Fig. 8(c)). The initial high dissipation and adhesion are primarily attributed to the capillary forces and viscous effects of water films on particle surfaces (Li et al., 2017). As temperature increases, the expulsion of surface water and interlayer water from clay minerals leads to the disappearance of these water films and causes mineral particles to contract and form tighter contacts. This results in a sharp decrease in adhesion and energy dissipation, leading to significant material hardening (Vishal et al., 2022). Synergistically, the pore structure remains relatively stable during this stage. The BET specific surface area and pore volume do not show significant directional changes, indicating no large-scale creation or destruction of the solid framework of shale.

Stage 2 (400-700 °C): Organic matter pyrolysis and viscoelastic softening. During this stage, due to organic matter pyrolysis and viscoelastic softening (Allan et al., 2016), the

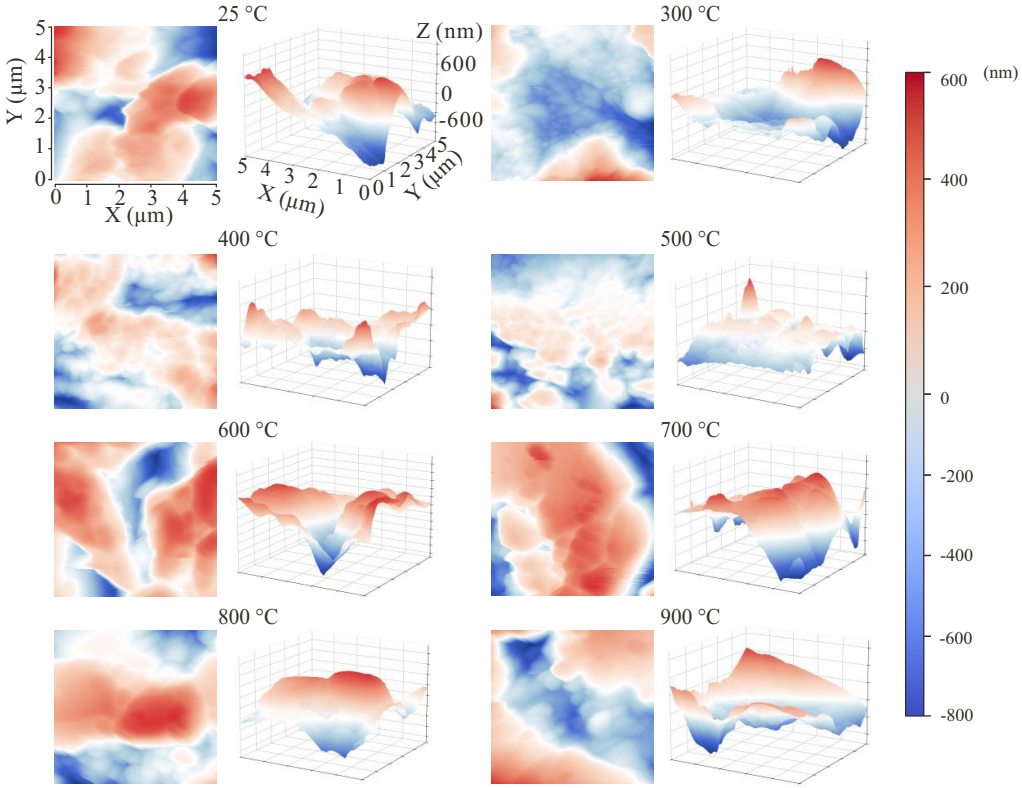

Fig. 6. AFM surface morphologies of heat-treated shale at various temperatures.

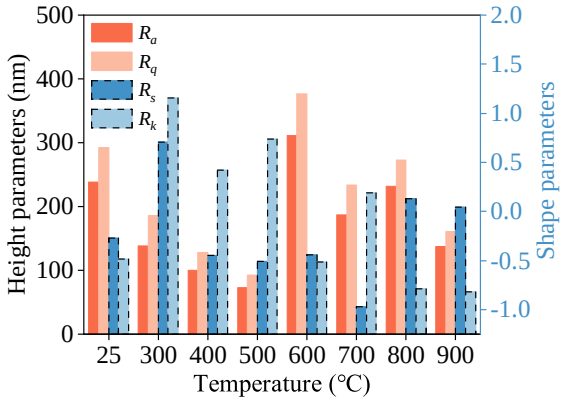

Fig. 7. Evolution of shale surface morphology with temperature.

E^* continuously decreases. Simultaneously, both energy dissipation and deformation surge (Fig. 8(a)), reaching their overall peaks at 600 °C (dissipation: 10,478.7 eV; deformation: 24.33 nm). The BET specific surface area drops sharply from 3.23 m^2/g (at 400 °C) to 1.22 m^2/g (at 700 °C), a reduction of over 60%. CO_2 pore size distribution data reveal a drastic reduction in micropore volume within this temperature range, especially for ultramicropores (< 1 nm). The dV/dD curve is significantly suppressed in the micropore section. The pore collapse caused by the expansion and pyrolysis of organic matter blocks the original nanopore network and prevents the entry of nitrogen molecules (Song et al., 2022).

Stage 3 (700-900 °C): Nanoscale fracturing from thermal cracking and rehardening. Above 700 °C, the modulus shows a second significant rebound, reaching 3.70 GPa at 800 °C, while the dissipation energy plummets from its 600 °C peak to 441.3 eV at 800 °C. Residual kerogen undergoes dehydrogenation and aromatic ring condensation, leading to interconnected and stacked structures that form larger, denser, and highly ordered graphite-like domains. This process causes the shale surface to reharden (Liang et al., 2024). The CO_2 pore size distribution data show an explosive increase in micropore volume at 800 °C, particularly for ultramicropores in the 0.5-0.8 nm range, with their dV/dD peak even surpassing that of the pristine sample (Fig. 9). This marks a turning point where the storage space of shale is renewed, a process of out with the old, in with the new, which is synchronized with mechanical rehardening.

Despite the drastic fluctuations in the block hardness of shale, the spatial clustering of hard and soft zones remains a persistent feature. Instead of homogenizing the material, the new heterogeneous system resulting from thermal treatment, mineral phase transitions, and thermal cracking progressively remodels the inherent spatial clustering pattern. This persistent heterogeneity is expected to decisively influence the fracture propagation patterns and preferential fluid pathways in thermally altered shale.

4.2 Synergistic spatial coupling of nanomechanical properties

To systematically reveal the evolution of the micromechanical structure of shale subjected to thermal treatment, a

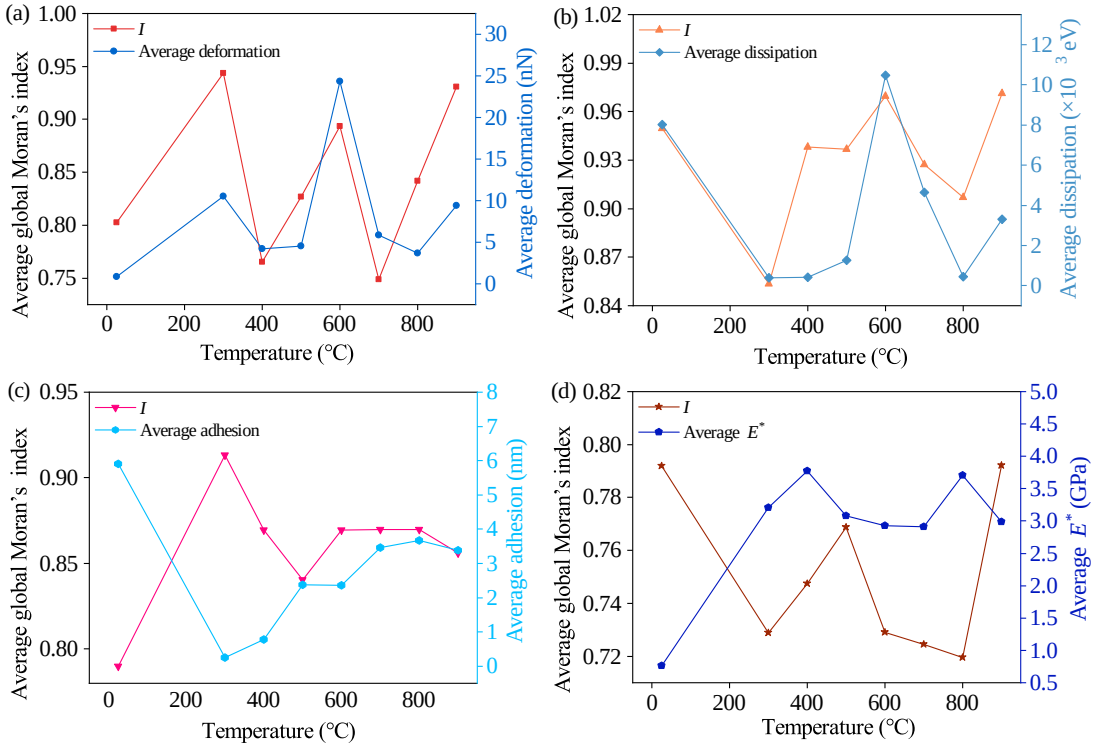

Fig. 8. Evolution of average nanomechanical properties and I of heat-treated shale with rising temperature: (a) Deformation, (b) dissipation, (c) adhesion and (d) E^*.

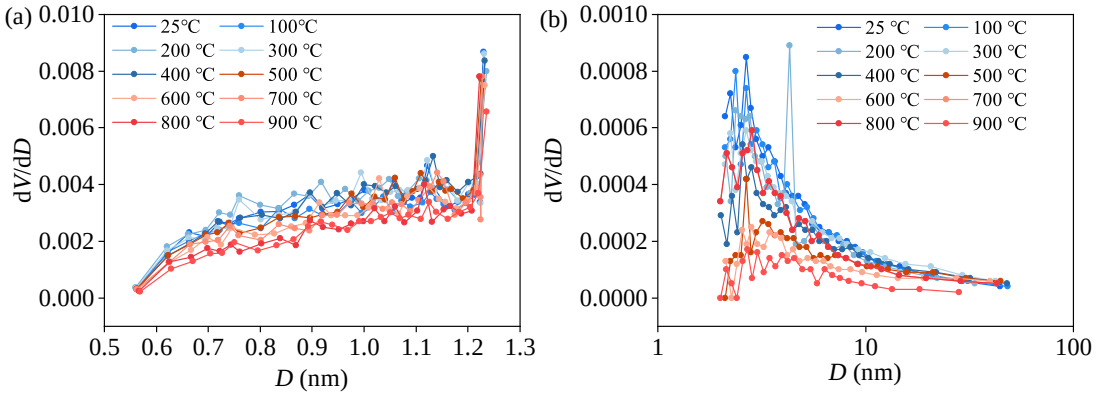

Fig. 9. Multiscale pore size distribution of thermally treated shale: (a) CO_2 adsorption and (b) N_2 adsorption.

multi-level spatial autocorrelation analysis was conducted on its nanomechanical property distributions. I analysis confirmed that all mechanical parameters exhibited a statistically highly significant positive spatial autocorrelation, indicating that the distribution of the mechanical properties of shale is not random but consistently presents an inherent clustering phenomenon. Building on this, the LISA analysis indicates that the thermal alteration of shale is not a single linear process, but rather a stage-wise evolutionary process dominated by different physicochemical mechanisms within specific temperature intervals.

In the initial low-temperature stage, the macroscopic mechanical properties of the shale undergo fundamental transformation. The overall stiffness of shale undergoes a sharp increase, with the average E^* soaring from approximately 0.76 GPa at 25 °C to a peak of about 3.77 GPa at 400 °C, an increase of nearly 400%. The adhesion force decreases rapidly from a high level (~5 nN) at room temperature to near zero as the surface loses its wettability, which further reduces the probe-sample adhesion. During this phase, not only does the physically adsorbed water film on particle surfaces disappear, but more importantly, a large amount of interlayer water is expelled from clay minerals such as montmorillonite and illite (Sun et al., 2016). The BET specific surface area remains relatively stable between 25 and 400 °C (e.g., 3.23 m^2/g at 400 °C), and the N_2 and CO_2 pore size distributions show no systematic changes. The LISA analysis provides decisive evidence for this dehydration effect. The dissipation analysis reveals that at 25 °C, the High-high (H-H) cluster occupies 17.9% of the area (Fig. 13), whereas at 400 °C, this cluster almost vanishes (Fig. 10). The area proportion of the Not

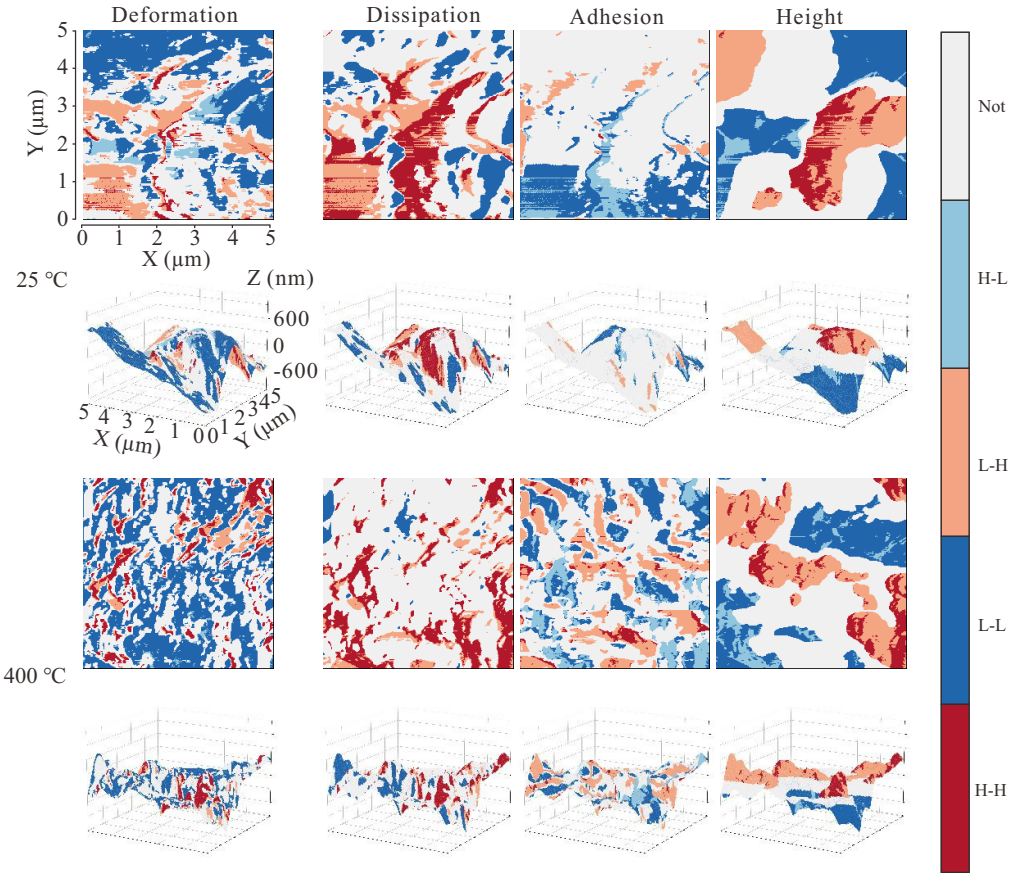

Fig. 10. Two- and three-dimensional visualization of LISA clusters in shale in Stage 2 (with 25 and 400 °C selected).

Significant (Not) regions surges from 57.3% at 25 °C to 73.3% at 400 °C (Fig. 13), constituting its overall peak. Macroscopic hardening at this stage is primarily driven by the removal of water and the dehydration-induced shrinkage of clay minerals, which compacts the entire mineral-organic framework (Cai et al., 2025). This confirms that the initial thermal effect is spatially dominated by physical changes on the surface.

The second stage, characterized by softening, marks a critical phase transition in the shale's property evolution. The mechanical response is reversed. The average energy dissipation reaches an absolute peak of 10,478 eV at 600 °C, and the average deformation also peaks at 24.3 nm. The average modulus decreased from 0.3771 to 0.2912 GPa, with a total decrease of about 22.8%, showing a trend of first decreasing rapidly, then decreasing slowly, and finally stabilizing. The adhesion force is lowest around 400 °C and then gradually recovers and increases, reaching the second highest value (~3 nN) at 700 °C. This is the result of a synergistic interaction between organic matter and inorganic minerals: High-maturity organic matter undergoes thermal softening, residual asphaltenes transform into a highly dissipative viscoelastic state, and clay minerals experience irreversible structural phase transitions in this temperature range (Mazumder et al., 2024). The BET specific surface area plummets to a nadir of 1.22 m^2/g at 700 °C as internal micropores are almost completely sealed, causing pore blockage. The viscoelastic transformation of the surface occurs synchronously with the physical blockage of internal pores. Quantitative LISA analysis shows that the micro-scale space becomes covered by large (Fig. 11), highly coherent Low-low (L-L) and Low-high (L-H) outliers, which represent soft matter, with their combined area reaching a peak of 35.7% (Fig. 13). The physical essence of this phenomenon is the superposition of softened organic matter regions and clay-mineral-rich regions weakened by dehydroxylation. The weakening of the inorganic matrix exacerbates the overall modulus decline. Studies have shown that layered silicates like montmorillonite and illite lose structural hydroxyl groups above 400 °C, transforming into amorphous metakaolin or mullite precursors, which reduces the load-bearing capacity of the mineral framework and decreases microporosity due to blockage by melts (Bai et al., 2017). This reveals a key challenge that *in-situ* conversion might face.

In the third stage, structural reorganization becomes the dominant phenomenon, leading to a fundamental reversal in the mechanical properties of shale. This rehardening process is a composite effect driven by the co-evolution of organic and inorganic matter. The adhesion force remains at a high and stable level (~3.6-3.7 nN), with some points even exceeding 7 nN (Fig. 13(a)). New microcracks and porous structures appear on the surface, increasing the actual contact area between the probe and the sample, thereby improving the measured adhesion force. At the organic matter level, the residual, softened viscoelastic material transforms into a rigid, porous framework through dehydrogenation and aromatic ring

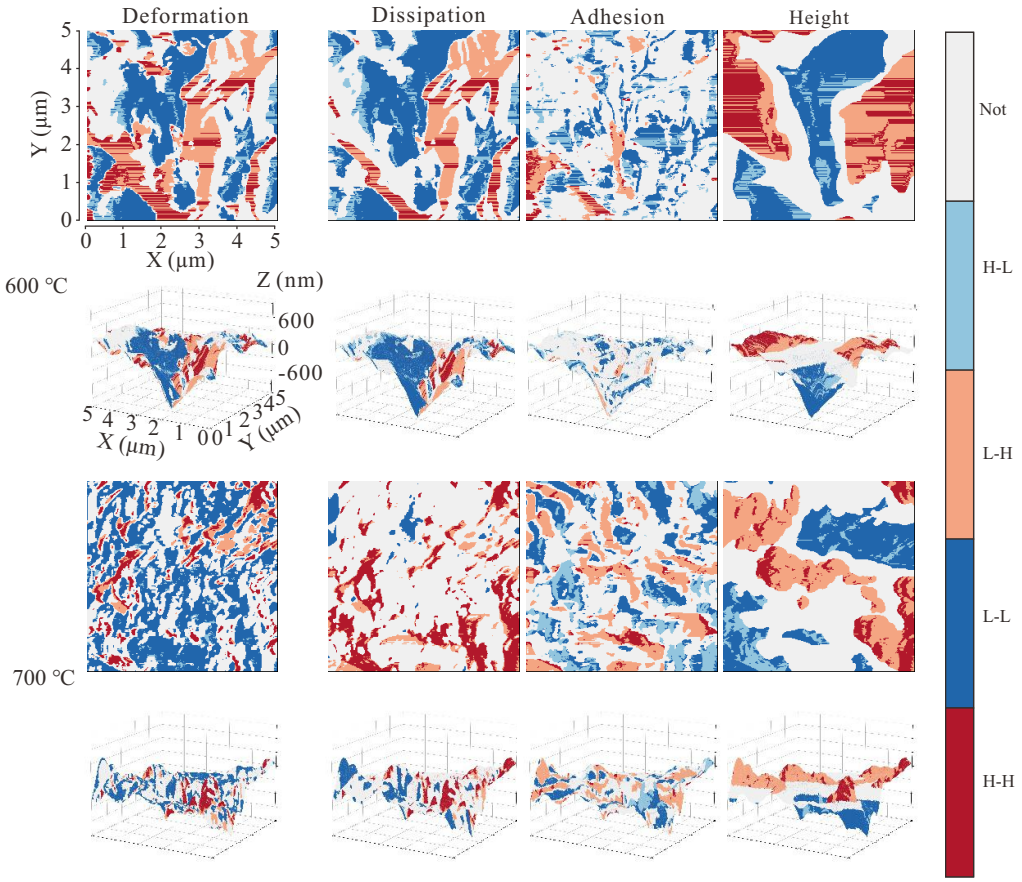

Fig. 11. Two- and three-dimensional visualization of LISA clusters in shale in Stage 2 (with 600 and 700 °C selected).

condensation (Hou et al., 2024). Meanwhile, at the inorganic mineral level, high-temperature sintering and mineral phase transitions occur (Karamov et al., 2022). These two processes collectively cause the average E^* to rebound to 3.70 GPa, reaches a peak of 3.70 GPa at 800 °C, and then decreases again to 2.99 GPa at 900 °C (Fig. 13(c)). However, the internal structure becomes unprecedentedly porous. The BET specific surface area soars to its absolute peak of 4.06 m^2/g at 800 °C, and CO_2 adsorption data confirm an explosive growth of a secondary micropore network. LISA analysis spatially decouples this phenomenon. The proportion of the Not region for dissipation again reaches a peak of 76.7% (Fig. 13(b)), proving that under vacuum (anoxic) conditions, the viscoelastic organic matter that previously acted as high-dissipation soft spots has completely transformed into a low-internal-friction structure, thereby spatially erasing its high-dissipation signature. On the other hand, the height (topography) LISA analysis shows that the L-L cluster area proportion reaches a high of 21.6% (Fig. 13(d)). This reveals the essence of rehardening: The high modulus corresponds directly to the formation of a composite framework of new rigid structures and sintered minerals, while low topography is the inevitable consequence of the intense mineral phase transitions and volume shrinkage that accompany this process.

4.3 Spatial coupling and geometric stability of shale

Bivariate LISA analysis is applied within this section to thoroughly examine the co-evolutionary processes and failure modalities occurring in shale subjected to vacuum pyrolysis. According to the materials science theory, the uniformity of a microstructure directly influences internal stress transfer and distribution. The SDR metric is introduced to quantify the uniformity of the geometric morphology of LISA spatial clusters, thereby assessing the geometric stability of the spatial configuration of each micro-domain. A lower SDR value signifies that a specific type of spatial cluster has a highly uniform morphology. This is conducive to forming a uniform stress field under load, avoiding stress concentrations caused by abrupt geometric changes. Conversely, a higher SDR value implies that the cluster morphology is highly heterogeneous, with both circular islands and elongated needle-like structures coexisting. These sharp geometric features act as natural stress concentrators under load, readily initiating the nucleation and propagation of microcracks (Griffith, 1921).

At 25 °C, the H-H clusters, representing the rigid mineral framework, undergo significant mechanical consolidation as their E^* increases from 4.7 to 8.3 GPa (Fig. 14). This is due to interlayer water expulsion from clay minerals, which shrinks their structures and creates tighter particle contacts. Geometric stability evolution reveals an unstable transition process. The

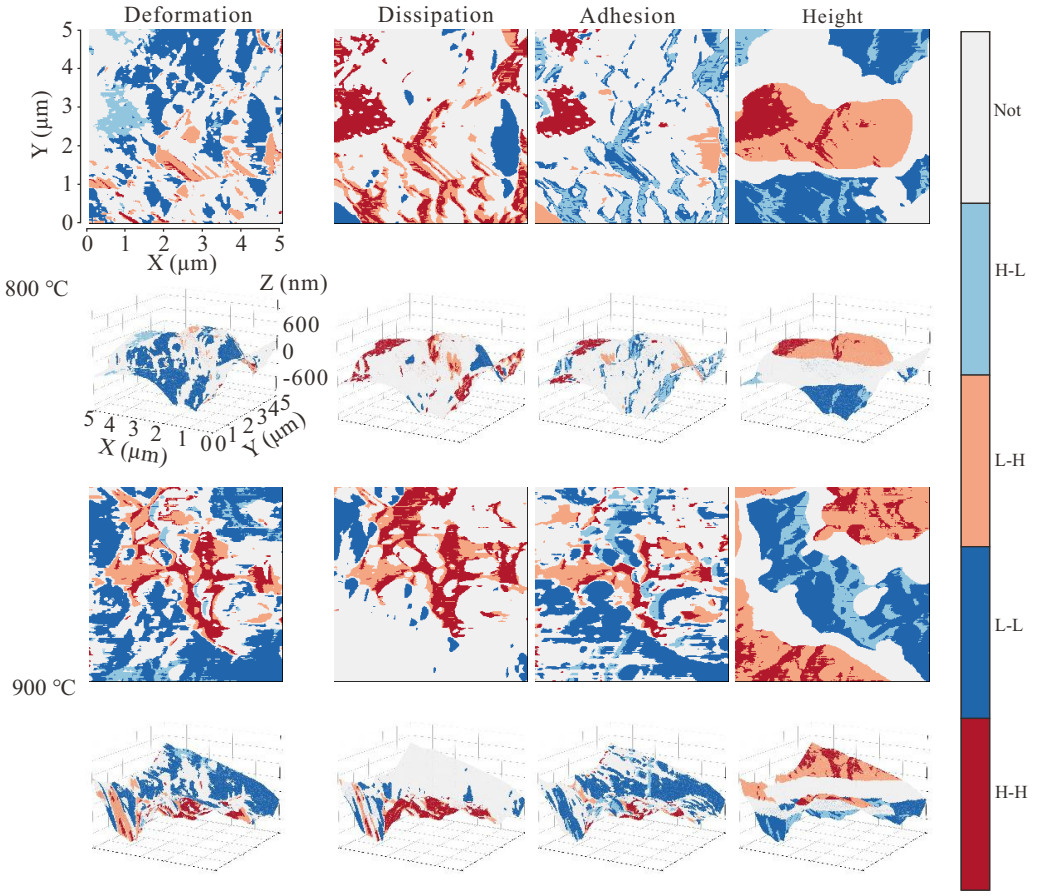

Fig. 12. Two- and three-dimensional visualization of LISA clusters in shale in Stage 3 (with 800 and 900 °C selected).

low-lying regions experience a dramatic topographic inversion, with their average height soaring from a depression to a significant peak of +141 nm (Fig. 15(a)). The L-L clusters, representing the soft organic phase, form a low-lying terrain with an average depth of -83 nm. The SDR values for High-low (H-L) and L-H increase during this stage, indicating that their geometric morphology becomes more less uniform (Fig. 15). This anomalous volume expansion, combined with the significant stiffening of the hard, high-altitude regions (E^* up to 8.3 GPa), suggests that while dehydration strengthens the mineral framework, it also disrupts the original organic-inorganic interface. This disruption pushes the system into its most geometrically chaotic state, which persists until 400 °C, when SDR values begin to decrease and a stable system gradually forms.

From 400 to 700 °C, the mechanical response of shale fundamentally reverses, driven by the synergistic weakening of organic and inorganic phases. LISA analysis shows that the average modulus of the soft, L-L clusters plummets to an extremely soft state ($E^* = 0.6$ GPa), with an extremely high SDR indicating highly non-uniform patch shapes. Their topography expands into a volcanic uplift reaching +143 nm (Fig. 16(c)), while surface interactions peak, with average energy dissipation exceeding 10,000 eV at 600 °C. Meanwhile, clay minerals undergo irreversible dehydroxylation, destroying their crystal lattice. This transforms them into weaker, amorphous materials, which reduces the load-bearing capacity of the mineral matrix (Zhang et al., 2024) and creates a highly undulating topographic pattern.

At 800 °C, thermal treatment reverses the correlation between surface mechanics and topography. Contrasting the previous pattern, a prominent low-lying deep-topography pattern emerges. LISA data show that the former soft regions (L-L clusters) reharden, their SDR value drops to a minimum (0.242), and their topography collapses from a +143 nm peak to a -233 nm abyss (Fig. 16(c)), forming a geometrically uniform porous network. The LISA spatial clusters associated with deformation (Fig. 16(b)) and dissipation (Fig. 16(c)), particularly the H-L and L-L combinations, exhibit a pronounced increase in average height, rising from negative or small values to larger positive values or near zero. This indicates that, at extremely high temperatures, the microscale deformation and energy dissipation capacity of shale are significantly enhanced or recover from previously lower states. The changes in adhesion (Fig. 16(a)) are more complex, showing two distinct trends: Some combinations (H-H, L-H) experience a decrease in adhesion, while others (H-L, L-L) display a marked increase, reflecting the differential adhesion behavior of various microscale contact points or mineral phases under high-temperature conditions. The decreasing SDR values for H-L and L-H outliers further suggest that residual organics and the mineral framework have formed a stable, ordered

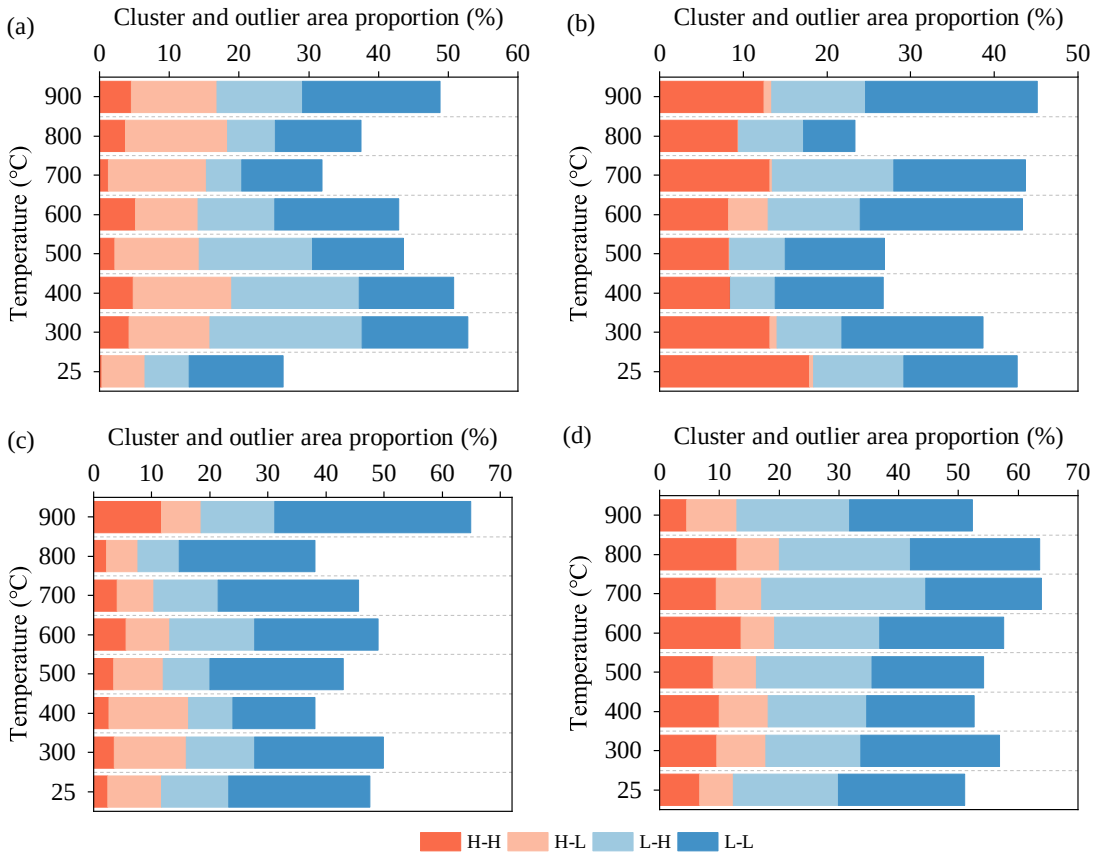

Fig. 13. Spatial clustering ratio of shale mechanical properties after heat treatment: (a) E^*-adhesion, (b) E^*-Dissipation, (c) E^*-Deformation and (d) E^*-Height.

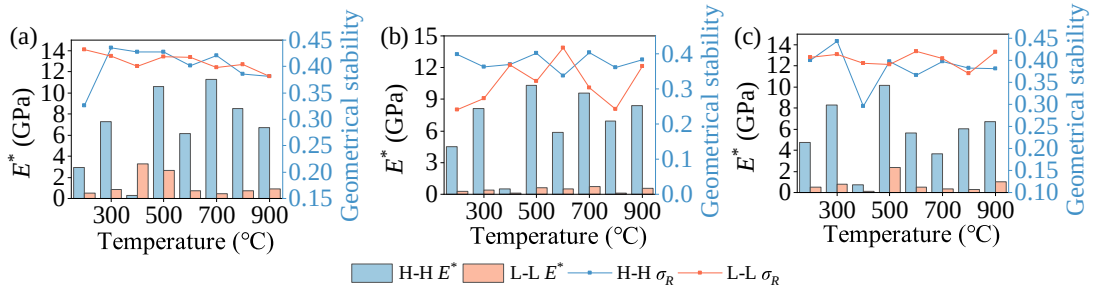

Fig. 14. Evolution of E^* and geometric stability of core outliers (H-H, L-L) in thermally treated shale (a) E^*-Adhesion, (b) E^*-Dissipation and (c) E^*-Deformation.

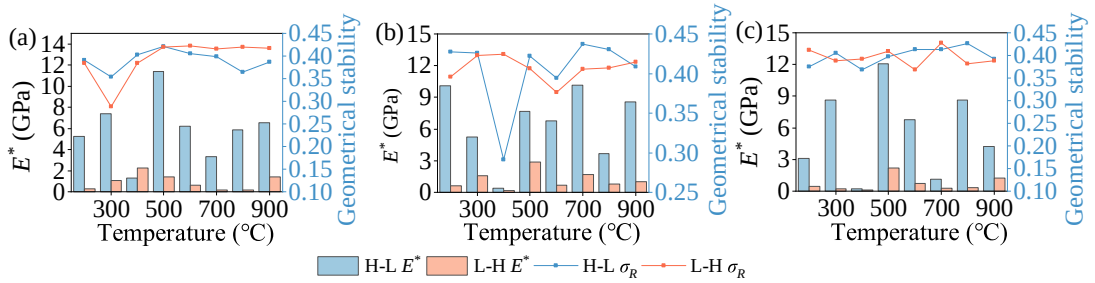

Fig. 15. Evolution of E^* and geometric stability of core outliers (H-L, L-H) in thermally treated shale: (a) E^*-Adhesion, (b) E^*-Dissipation and (c) E^*-Deformation.

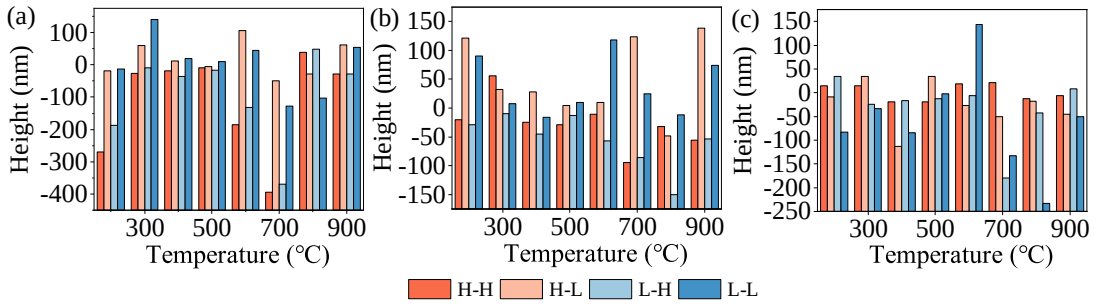

Fig. 16. Average morphological height evolution of LISA spatial clusters in thermally treated shale: (a) E^*-Adhesion, (b) E^*-Deformation and (c) E^*-Dissipation.

interface, creating a new, deep porous structure. Overall, the LISA spatial clusters of shale demonstrate high sensitivity to temperature variations in the 800-900 °C range, particularly for the deformation and dissipation properties.

At higher temperatures, the shale exhibits irreversible damage. Upon reaching 900 °C, the depressions are significantly backfilled (rebounding to -49 nm), as mineral sintering causes structural collapse. After the peak geometric order at 800 °C, SDR values for all outliers rebound significantly at 900 °C. This confirms that the microstructure has transitioned from an ordered state to one of chaotic geometry and random damage, leading to a comprehensive deterioration of micro-phase mechanical properties. This observation directly explains why storage capacity is permanently destroyed at excessively high temperatures.

5. Conclusions

This study focused on the local topology of deep shale thermal transformation and systematically discovered the spatial localization patterns of the nanomechanical properties and floor structure of Longmaxi Formation carbonaceous shales subjected to transient thermal treatment (25-900 °C). By innovatively combining gas adsorption, AFM high-resolution mapping, and multi-level spatial statistical analysis (LISA and SDR), a unique three-stage hierarchical model of lymphoma-softening-relymphoma during shale thermal transformation was identified. From the findings, the following conclusions could be drawn:

1) The thermal alteration of shale is not a single, linear process but follows a distinct, staged pathway dominated by specific physicochemical mechanisms. Unlike a monotonic accumulation of damage, the evolution of shale exhibits a unique three-stage pattern of hardening-softening-rehardening. All macroscopic and microscopic responses of shale under thermal stress are the macroscopic manifestation of the synergistic interactions between its organic components and inorganic minerals in different temperature regimes. This ranges from the initial stage of physical dehydration and framework consolidation (25-400 °C), to the softening stage characterized by organic matter softening and clay weakening via dehydroxylation (400-700 °C), and finally to the rehardening stage involving dehydrogenation and the condensation of organic matter and sintering of inorganic minerals (700-900 °C). The mechanical and geometric evolution at each stage is the result of the interaction and co-evolution of these two components.
2) LISA spatial analysis reveals that the evolution of macroscopic properties is a direct manifestation of the synergistic evolution of microscopic phases and the reorganization of their spatial patterns. By decoupling the mechanical, geometric, and morphological evolution of different spatial clusters, we traced the process from initial interfacial destabilization caused by dehydration (25-400 °C); to abrupt uplifts (up to +143 nm) and depressions triggered by residual organic matter (400-700 °C); to collapse (down to -233 nm) and the genesis of a new porous network driven by high temperatures (700-900 °C); culminating in structural destruction caused by mineral sintering. Notably, at 800 °C, the systematic decrease in geometric instability and the maximization of interfacial integrity confirm the formation of a microstructure that is geometrically highly uniform and solidified through multi-phase synergy.
3) The temperature range of 400-500 °C is identified as the optimal temperature threshold for the *in-situ* pyrolysis and alteration of shale, providing a critical optimization window for thermal recovery processes that balances efficiency, economy, and safety. While higher temperatures (e.g., 800 °C) can theoretically achieve maximum pore reconstruction, in engineering practice, they face immense energy consumption, which undermines their economic feasibility. The milder temperature range of 400-500 °C can both effectively initiate the pyrolysis of organic matter, achieving the core goal of resource conversion, and significantly reduce engineering costs. This temperature range provides robust micro-mechanistic support for maximizing the benefits of shale resource development through precise temperature control.

Despite the above results, it is worth noting that achieving and maintaining a temperature range of 400-500 °C for extended periods in actual deep shale reservoirs will face significant engineering challenges. These include, but are not limited to, the development of efficient thermal injection technologies, the control of heat loss, and the impact of high temperatures on the durability of existing reservoir completion

and production equipment. Future research needs to further explore strategies to overcome these engineering obstacles.

Acknowledgements

This work was supported by the Science and Technology Research Program of Chongqing Municipal Education Commission (No. KJZD-K202401205); Research and Innovation Project for Postgraduate Students of Chongqing Three Gorges University (No. YISKY25044). We further acknowledge the computational support provided by the Department of Earth Resources Engineering, Faculty of Engineering, Kyushu University, for the data processing and analysis.

Conflict of interest

The authors declare no competing interest.

References

Allan, A. M., Clark, A. C., Vanorio, T., et al. On the evolution of the elastic properties of organic-rich shale upon pyrolysis-induced thermal maturation. Geophysics, 2016, 81(3): 263-281.

Anselin, L. Local indicators of spatial association—LISA. Geographical Analysis, 1995, 27(2): 93-115.

Bai, F., Sun, Y., Liu, Y., et al. Evaluation of the porous structure of Huadian oil shale during pyrolysis using multiple approaches. Fuel, 2017, 187(1): 1-8.

Brunauer, S., Emmett, P. H., Teller, E. Adsorption of gases in multimolecular layers. Journal of the American Chemical Society, 1938, 60(2): 309-319.

Cai, J., Wood, D., Hajibeygi, H., et al. Multiscale and multiphysics influences on fluids in unconventional reservoirs: Modeling and simulation. Advances in Geo-Energy Research, 2022a, 6(2): 91-94.

Cai, J., Zhao, L., Zhang, F., et al. Advances in multiscale rock physics for unconventional reservoirs. Advances in Geo-Energy Research, 2022b, 6(4): 271-275.

Cai, Z., Zhao, L., Ma, J., et al. Evolution of the elastic properties of lacustrine organic shales under different thermal maturity conditions. Science China Earth Sciences, 2025, 68: 781-802.

Chen, X., Tang, X., Liu, C., et al. Implications of temperature for the modification of high-overmature shale reservoirs: Experimental and numerical analysis. SPE Journal, 2024, 29(8): 4218-4231.

Chen, X., Tang, X., Zhang, R., et al. Changes in shale microstructure and fluid flow under high temperature: Experimental analysis and fluid-structure interaction simulation. Petroleum Science, 2025, 22(4): 1699-1711.

Cheng, B., Li, S., Xu, J., et al. Gaseous hydrocarbons cracking in shale: Mechanism, impact and resource significance. Earth-Science Reviews, 2025, 270: 105211.

Cliff, A. D., Ord, J. K. Spatial Autocorrelation. London, UK, Pion, 1973.

Dai, J., Raza, A., Wang, T., et al. Impact of CO_2-Brine-Shale interaction on wettability change at reservoir temperature and pressure via AFM characterization. Energy & Fuels, 2024, 38(21): 21042-21051.

Derjaguin, B., Muller, M., Toporov, Y. P. Effect of contact deformations on the adhesion of particles. Journal of Colloid and Interface Science, 1975, 53(2): 314-326.

Dickinson, L. R., Suijkerbuijk, B. M. J. M., Berg, S., et al. Atomic force spectroscopy using colloidal tips functionalized with dried crude oil: A versatile tool to investigate oil-mineral interactions. Energy & Fuels, 2016, 30(11): 9193-9202.

Emmanuel, S., Eliyahu, M., Day-Stirrat, R. J., et al. Impact of thermal maturation on nano-scale elastic properties of organic matter in shales. Marine and Petroleum Geology, 2016, 70: 175-184.

Emmanuel, S., Ruarri, J. M. E., Stirrat, D., et al. Softening of organic matter in shales at reservoir temperatures. Petroleum Geoscience, 2017, 23(2): 262-269.

Feng, G., Zhang, L., Yan, J., et al. Lithofacies-based analysis of pore structure characteristics and controlling factors of shale reservoirs: A case study of the second member of the Kongdian Formation in the Cangdong Sag, Bohai Bay Basin, China. Marine and Petroleum Geology, 2025, 182: 107575.

Giergiel, M., Zapotoczny, B., Czyzynska-Cichon, I., et al. AFM image analysis of porous structures by means of neural networks. Biomedical Signal Processing and Control, 2022, 71: 103097.

Goodarzi, M., Rouainia, M., Aplin, A., et al. Predicting the elastic response of organic-rich shale using nanoscale measurements and homogenisation methods. Geophysical Prospecting, 2017, 65(6): 1597-1614.

Graham, S. P., Rouainia, M., Aplin, A. C., et al. Geomechanical characterisation of organic-rich calcareous shale using AFM and nanoindentation. Rock Mechanics and Rock Engineering, 2021, 54: 303-320.

Griffith, A. A. VI. The phenomena of rupture and flow in solids. Philosophical Transactions of the Royal Society of London, 1921, 221(582-593): 163-198.

Hou, Y., Yu, R., Li, J., et al. Molecular structure characterization of kerogen in contact metamorphic shales: Insights into the effect of graphitization on organic matter pores. AAPG Bulletin, 2024, 108(4): 633-662.

Iqbal, M. A., Rezaee, R., Smith, G., et al. Shale lithofacies controls on porosity and pore structure: An example from Ordovician Goldwyer Formation, Canning Basin, Western Australia. Journal of Natural Gas Science and Engineering, 2021, 89: 103888.

Jiang, X., Han, X., Cui, Z. New technology for the comprehensive utilization of Chinese oil shale resources. Energy, 2007, 32(5): 772-777.

Karamov, T., White, V., Idrisova, E., et al. Alterations of carbonate mineral matrix and kerogen micro-structure in domanik organic-rich shale during anhydrous pyrolysis. Minerals, 2022, 12(7): 870.

Khatibi, S., Ostadhassan, M., Tuschel, D., et al. Raman spectroscopy to study thermal maturity and elastic modulus

of kerogen. International Journal of Coal Geology, 2018, 185(2): 103-118.

Li, C., Ostadhassan, M., Guo, S., et al. Application of peakforce tapping mode of atomic force microscope to characterize nanomechanical properties of organic matter of the Bakken Shale. Fuel, 2018, 233: 894-910.

Li, J., Li, X., Wu, K., et al. Thickness and stability of water film confined inside nanoslits and nanocapillaries of shale and clay. International Journal of Coal Geology, 2017, 179(15): 253-268.

Li, J., Shan, X., Song, X., et al. Evaluation of the organic matter product of Huadian oil shale during pyrolysis using multiple approaches: Guidance for the *in situ* conversion of oil shale. Journal of Analytical and Applied Pyrolysis, 2022, 167: 105656.

Li, Z., Duan, Y., Peng, Y., et al. A laboratory study of microcracks variations in shale induced by temperature change. Fuel, 2020, 280(15): 118636.

Liang, Z., Jiang, Z., Xue, Z., et al. Molecular structure and evolution mechanism of shale kerogen: Insights from thermal simulation and spectroscopic analysis. Journal of Analytical and Applied Pyrolysis, 2024, 181: 106648.

Liu, Q., Chen, T., Zhang, H., et al. Experimental investigation of permeability evolution in deep reservoirs under true triaxial stress: A review. Gas Science and Engineering, 2025, 144: 205739.

Loucks, R. G., Reed, R. M., Ruppel, S. C., et al. Spectrum of pore types and networks in mudrocks and a descriptive classification for matrix-related mudrock pores. AAPG Bulletin, 2012, 96: 1071-1098.

Lovric, M. International Encyclopedia of Statistical Science. Berlin, Germany, Springer, 2025.

Mazumder, M., Bal, A., Tripathy, A., et al. Multiscale assessment of transformation in pore system of shale during combustion: An insight into poromechanical response and sorption dynamics. Energy & Fuels, 2024, 38(18): 17510-17524.

Moran, P. A. P. Notes on continuous stochastic phenomena. Biometrika, 1950, 37(1-2): 17-23.

Paruchuri, A., Wang, Y., Gu, X., et al. Machine learning for analyzing atomic force microscopy (AFM) images generated from polymer blends. Digital Discovery, 2024, 3(12): 2533-2550.

Saif, T., Lin, Q., Bijeljic, B., et al. Microstructural imaging and characterization of oil shale before and after pyrolysis. Fuel, 2017, 197: 562-574.

Song, D., Wu, C., Tuo, J. Relationships between organic structure carbonization and organic pore destruction at the overmatured stage: Implications for the fate of organic pores in marine shales. Energy & Fuels, 2022, 36(13): 6906-6921.

Song, Y., Li, Z., Jiang, Z., et al. Progress and development trend of unconventional oil and gas geological research. Petroleum Exploration and Development, 2017, 44(4): 675-685.

Sun, C., Nie, H., Su, H., et al. Porosity, permeability and rock mechanics of Lower Silurian Longmaxi Formation deep shale under temperature-pressure coupling in the Sichuan Basin, SW China. Petroleum Exploration and Development, 2023, 50(1): 85-98.

Sun, Q., Zhang, W., Qian, H. Effects of high temperature thermal treatment on the physical properties of clay. Environmental Earth Sciences, 2016, 75, 610.

Vishal, V., Rizwan, M., Mahanta, B., et al. Temperature effect on the mechanical behavior of shale: Implication for shale gas production. Geosystems and Geoenvironment, 2022, 1(4): 100078.

Vranjes-Wessely, S., Misch, D., Kiener, D., et al. High-speed nanoindentation mapping of organic matter-rich rocks: A critical evaluation by correlative imaging and machine learning data analysis. International Journal of Coal Geology, 2021, 247(1): 103847.

Wang, J., Zhang, Y., Liu, J., et al. Shale weak cementation model and elastic modulus prediction based on nanoindentation experiment. Petroleum Science, 2025, 22(5): 2123-2141.

Wang, L., Zhao, Y., Yang, D. Evolution of permeability and mesostructure of oil shale exposed to high-temperature water vapor. Fuel, 2021, 290(15): 119786.

Wang, Q., Wang, T., Zhong, P., et al. Study of the surface pore structure and micromechanical properties of the Longmaxi shale. Petroleum Science Bulletin, 2023a, 8(5): 626-636. (in Chinese)

Wang, Y., Cheng, H. Advances in microscopic pore structure characterization of fine-grained mudrocks. Energy & Fuels, 2023, 37(3): 1495-1510.

Wang, Z., Ma, Z., Zheng, L., et al. Dynamic evolution characteristics of the "source-reservoir" integration of gray marl and its geological significance to unconventional gas: Insights from pyrolysis experiments. Petroleum Science, 2023b, 20(2): 705-720.

Yan, H., Zhou, T., Zhou, X., et al. Non-monotonic evolution and spatial reorganization mechanism of thermally induced micro-damage in sandstone. Advances in Geo-Energy Research, 2025, 17(2): 135-148.

Zargari, S., Wilkinson, T. M., Packard, C. E., et al. Effect of thermal maturity on elastic properties of kerogen. Geophysics, 2016, 81(2): M1-M6.

Zhang, H., Jia, X., Wu, J., et al. Impact of inherent minerals on isothermal pyrolysis of oil shale: Characteristics and kinetics. Journal of Analytical and Applied Pyrolysis, 2025, 191: 107231.

Zhang, L., Yang, D., Zhao, K., et al. Investigation of high-temperature effects on the strengthening and degradation of mechanical property in sandstone. Applied Energy, 2024, 357(1): 122532.

Zhang, Y., Lebedev, M., Al-Yaseri, A., et al. Nanoscale rock mechanical property changes in heterogeneous coal after water adsorption. Fuel, 2018, 218: 23-32.